Journal of Engineering for Gas Turbines and Power. Received July 03, 2024;
Accepted manuscript posted July 22, 2024. doi:10.1115/1.4066047

Liquid Cooling of Fuel Cell Powered Aircraft: The Effect of Coolants on Thermal Management

Adam C. Frey, first author
University of Bath
University of Bath, Department of Mechanical Engineering, Bath, BA2 7AY, United Kingdom
af718@bath.ac.uk

David Bosak, second author
GKN Aerospace
GKN Aerospace, Global Technology Centre, Filton, BS34 6FB, United Kingdom
david.bosak@gknaerospace.com

Joseph Stonham, third author
GKN Aerospace
GKN Aerospace, Global Technology Centre, Filton, BS34 6FB, United Kingdom
joseph.stonham@gknaerospace.com

Carl M. Sangan, fourth author
University of Bath
University of Bath, Department of Mechanical Engineering, Bath, BA2 7AY, United Kingdom
C.M.Sangan@bath.ac.uk

Oliver J. Pountney, fifth author[1]
University of Bath
University of Bath, Department of Mechanical Engineering, Bath, BA2 7AY, United Kingdom
O.J.Pountney@bath.ac.uk

[1] Oliver J. Pountney is the corresponding author.

Journal of Engineering for Gas Turbines and Power. Received July 03, 2024;
Accepted manuscript posted July 22, 2024. doi:10.1115/1.4066047

ABSTRACT

Electric propulsors powered by Proton Exchange Membrane Fuel Cells (PEMFCs) offer a net zero solution to aircraft propulsion. Heat generated by the PEMFCs can be transferred to atmospheric air via a liquid cooling system; however, the cooling system results in parasitic power and adds mass to the propulsion system, thereby affecting system specific power. The design of the cooling system is sensitive to the choice of liquid coolant and so informed coolant selection is required if associated parasitic power and mass are to be minimized.

Two approaches to selection of coolants for PEMFC-powered aircraft are presented in this paper for operating temperatures in the range 80-200°C (this covers low, intermediate, and high temperature PEMFCs). The first approach uses a Figure of Merit (FoM) alongside minimum and maximum operating temperature requirements. The FoM supports the selection of coolants that minimize pumping power and mass while maximizing heat transfer rate. The second approach uses a cooling system model to select "Pareto efficient" coolants. A hybrid-electric aircraft using a PEMFC stack is used as a representative case study for the two approaches.

Hydrocarbon-based coolants are shown to be favorable for the case study considered here (aromatics for PEMFCs operating at <130°C and aliphatics for PEMFCs operating at >130°C). As the PEMFC operating temperature increases, the parasitic power and mass of the Thermal Management System (TMS) decreases. Operating at elevated temperatures is therefore beneficial for liquid cooled PEMFC-powered aircraft. Nevertheless, there are diminishing performance gains at higher operating temperatures.

1. INTRODUCTION

The International Air Transport Association (IATA) and International Civil Aviation Organization (ICAO) have proposed targets for achieving net zero carbon dioxide emissions in aviation by 2050 [1,2]. These targets are driving research and development

Journal of Engineering for Gas Turbines and Power. Received July 03, 2024;
Accepted manuscript posted July 22, 2024. doi:10.1115/1.4066047

of low emission aircraft propulsion technologies. The following are the three leading solutions for net zero aircraft propulsion: (1) hydrogen fuel cells, (2) hydrogen combustion, and (3) Sustainable Aviation Fuel (SAF) combustion [3]. The concept of a hydrogen-powered aircraft is not a recent development. In 1937, Heinkel bench-tested the first jet engine (HeS 1), which operated with hydrogen owing to their accelerated development program [4]. The first flight of a hydrogen combustion powered-aircraft took place in 1956, conducted by the US Air Force using a modified B-57 twin-engine bomber [5]. Since the 1950s, kerosene has been the preferred aviation fuel due to its availability, cost, low freezing point, and its suitable combustion properties [6,7]. However, kerosene cannot meet net zero emission targets; alternative propulsion systems which achieve net zero carbon dioxide emissions must be developed. One of the leading candidates is a hydrogen fuel cell, electricity is generated through an electrochemical reaction between hydrogen and oxygen. This electricity is then utilized to produce thrust on the aircraft via an electric-powered propulsor. Hydrogen fuel cells achieve superior efficiency, cost reductions, and a lack of particulate and nitrogen oxide emissions compared to both hydrogen and SAF combustion [8,9].

Initially designed for space power plants, fuel cell technology was later adapted for and further refined within the automotive industry. Proton Exchange Membrane Fuel Cells (PEMFCs) are the most common fuel cell and display favorable traits for aerospace applications. For example, PEMFCs operating at 80°C are commercially mature, they operate with a high efficiency, and have surpassed 5000 hours of continuous and transient operation (which betters early jet engine technology) [10-13].

Journal of Engineering for Gas Turbines and Power. Received July 03, 2024;
Accepted manuscript posted July 22, 2024. doi:10.1115/1.4066047

PEMFCs are categorized as Low Temperature (LT), Intermediate Temperature (IT), and High Temperature (HT). Typical temperature ranges are: LT 80-100°C, IT 100-120°C, and HT 120-250°C [14-16]. Note that these temperature ranges vary somewhat in the wider literature. In this study, the maximum operating temperature is set at 200°C due to the low Technology Readiness Level (TRL) of PEMFCs exceeding 200°C. Figure 1 outlines the key components in a PEMFC and the electrochemical reaction, the byproduct being heat and water.

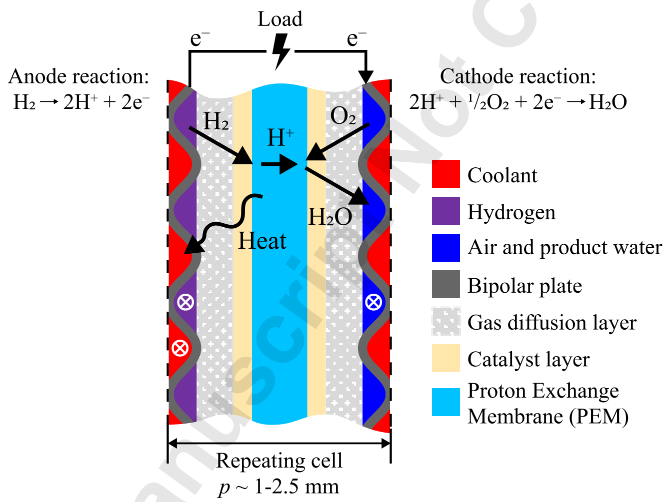

Figure 1: Schematic of a Proton Exchange Membrane Fuel Cell (PEMFC) and the electrochemical reaction.

While hydrogen fuel cells show promise, the Thermal Management System (TMS) poses a critical challenge due to the associated parasitic power and mass. The TMS challenge with fuel cell propulsion systems is highlighted by the system specific power [11]. Achieving a system specific power that approaches and exceeds 2 kW/kg is crucial for the market success of regional aircraft (80-165 passengers, <2000 km range,

Journal of Engineering for Gas Turbines and Power. Received July 03, 2024;
Accepted manuscript posted July 22, 2024. doi:10.1115/1.4066047

and 0.44-0.72 Mach) [17]. Regional aircraft present market opportunities for fuel cell propulsion systems because they contribute to at least 30% of aviation's carbon dioxide emissions [17]. Estimates place fuel cell propulsion system specific power at ~ 1 kW/kg [11]. To enhance the system specific power and consequently approach the 2 kW/kg target, there are two primary objectives: first, increase the power output without compromising system efficiency, and second reduce the mass of the system. These objectives are strongly dependent on the TMS.

Figure 2 illustrates the transfer of the heat generated by a PEMFC stack to the terminal sink (atmospheric air) via a liquid cooling system installed within the aircraft structure. Note that phase-change cooling is beyond the scope of this paper (the interested reader is directed to [18] for associated information). The key components of the liquid cooling system are the radiator, pump, piping and coolant. For a regional aircraft, the cooling system must transfer megawatts of heat to the surrounding air. It must do this while minimizing associated parasitic power and mass to ensure that the specific power level of the propulsion system is adequate. The design of the cooling system (and thereby its parasitic power and mass) is sensitive to the choice of coolant, and so it is important to understand the implications of coolant properties on the cooling system so that an informed selection can be made.

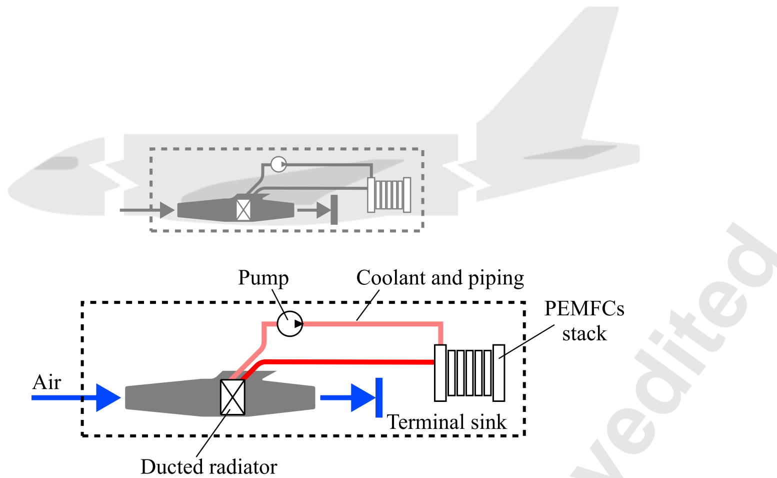

Figure 2: Notional liquid cooled proton exchange membrane fuel cell propulsion system with a ducted radiator installed under the wing.

This paper develops an approach for informed coolant selection and makes recommendations for PEMFCs which require pure hydrogen and operate at temperatures in the range 80-200°C. A review of literature pertinent to coolant selection in the context of PEMFCs is provided in Section 2. A new Figure of Merit (FoM) is outlined in Section 3 and used to screen coolants for high specific heat transfer rate and low pumping power. Section 4 outlines a cooling system model that enables a more refined coolant selection method than the FoM; the model is subsequently used to carry out a sensitivity study on relevant boundary conditions. Liquid coolants are selected via model-informed Pareto fronts for different PEMFC operating temperatures in Section 5. Selection “use cases” for favorable coolants are also included in Section 5 and compared against those obtained from the FoM. Finally, Section 6 addresses the main conclusions. Note that coolant selection is less critical in jet engines as heat energy is dissipated

Journal of Engineering for Gas Turbines and Power. Received July 03, 2024;
Accepted manuscript posted July 22, 2024. doi:10.1115/1.4066047

directly to air; nevertheless, the approach presented in this paper could be readily applied to jet engine subsystems.

2. LITERATURE REVIEW

From an operational standpoint, the ideal coolant should possess thermophysical properties that ensure favorable performance across the entire operating temperature range, while also adhering to safety requirements. The adequacy of thermophysical properties is mainly dependent on the density, dynamic viscosity, thermal conductivity, and specific heat capacity. There are various coolant compositions that have been proposed in the broader literature [19]. Most suppliers of coolants offer hydrocarbons, silicones, pure glycols, and aqueous solutions [20,21]. For this reason, these are included in Figure 3. Aqueous coolants encompass any coolant containing water, while hydrocarbons can be further classified based on chemical structure (details not discussed here) into aliphatic and aromatic types. A coolant is classified as "other HC" (HC – hydrocarbon) if the exact composition is unknown. Recently, much of the literature on coolants has focused on the development of nanofluids [22]. These are not assessed in this paper (and therefore not presented in the ontological plot in Figure 3) due to limited commercial availability and practical challenges [23], such as degradation of nanofluid coolant properties through particle agglomeration [24].

Journal of Engineering for Gas Turbines and Power. Received July 03, 2024;
Accepted manuscript posted July 22, 2024. doi:10.1115/1.4066047

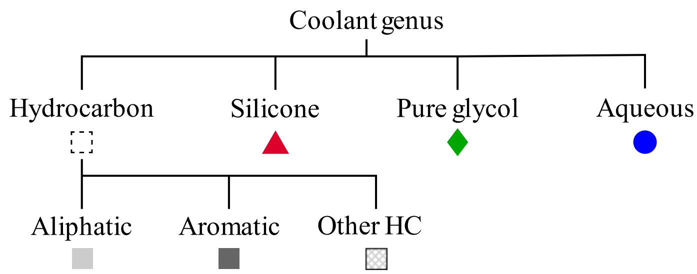

Figure 3: Coolant ontology. Note – Aliphatic and Aromatic Hydrocarbons may comprise blends, and 'Other HC' categorizes Hydrocarbons of unknown composition.

The critical requirements of a coolant for a liquid cooled PEMFC operating in an aircraft are detailed in Table 1. These are critical requirements because a coolant must not freeze, boil, auto-ignite, or short circuit across the operating temperature range. The thresholds in Table 1 are:

1. <u>Min. temperature:</u> The minimum temperature is taken as the freezing point of Jet A-1 [25]. This is a pragmatic threshold as conventional aircraft safely operate with Jet A-1 in subzero conditions. The reader is referred to Barron's work on aircraft lubrication oil in subzero conditions for further context [26].
2. <u>Max. temperature:</u> The maximum temperature is defined by the PEMFC operating temperature (80-200°C) plus a margin of 10°C. A 10°C margin is typically used for jet fuel autoignition prevention; the same margin is adopted here but for the boiling point [27]. For example, to select a suitable coolant for a PEMFC stack that operates at 80°C, the boiling point must exceed 90°C. Some of the coolants considered in this study have flash points below the PEMFC operating temperature. For context, Jet A-1 has a minimum flash point of 38°C at ~1 bar but is deemed safe for operation above this temperature because of ignition

Journal of Engineering for Gas Turbines and Power. Received July 03, 2024;
Accepted manuscript posted July 22, 2024. doi:10.1115/1.4066047

prevention measures [25,28]. For this reason, the boiling point (rather than flash point) is also employed as the threshold for flammable coolants here.

3. Electrical conductivity: The coolant flows through channels, typically pressed into bipolar plates. An electrically conductive coolant will cause current leakage and short circuiting between the electrodes on these bipolar plates. It is therefore a critical requirement to keep the conductivity below 5 μS/cm [29].

Table 1: Critical system level requirements for liquid coolants inside a fuel cell powered aircraft.

Property	Threshold	Unit
Min. temperature	≤-47	°C
Max. temperature	≥[80:200]+10	°C
Electrical conductivity	<5	μS/cm

The effect of coolants on the TMS is the purpose of this paper. Hence, noncritical operational requirements such as chemical compatibility, maintenance requirements, environmental impact, and regulation are not addressed here. It is recommended that such considerations are evaluated prior to the widespread adoption of a particular coolant.

3. FIGURE OF MERIT

Selecting a coolant based purely on its thermophysical properties at expected operating temperatures is desirable in terms of expediency. To do so, a parameter exclusively composed of thermophysical properties must be developed.

Journal of Engineering for Gas Turbines and Power. Received July 03, 2024;
Accepted manuscript posted July 22, 2024. doi:10.1115/1.4066047

In 1942, Mouromtseff proposed a 'factor' which assesses the ability of a fluid to transfer heat by convection; it is derived from the Dittus-Boelter Nusselt number correlation for turbulent internal flow by grouping fluid properties [30]. Mouromtseff's 'factor' can be rederived for other practical cases by using the corresponding Nusselt number correlation. However, it is unsuitable for selecting coolants with a low pumping power and mass as they are not considered in its derivation. Newton's law of cooling shows that convective heat transfer rate is dependent on the surface area, temperature, and heat transfer coefficient. Hence, the selection of a coolant via Mouromtseff's approach does not necessarily maximize the heat transfer rate, as this 'factor' only considers the heat transfer coefficient.

In 1957, Bonilla proposed several FoMs for coolant selection in the nuclear industry [31]. Bonilla's FoM captures both the heat transfer rate and pumping power, *i.e*. for a given heat transfer rate it enables coolants which have low pumping powers to be selected. Following Bonilla, Lenert *et al.* (2012) and Ehrenpreis *et al.* (2020) both developed similar FoMs which attempt to minimize pumping power for a given heat transfer rate [32,33]. In addition, Ghajar and Tang (1994) proposed several ratios to assess the relative difference in performance between coolants [34]. FoMs for coolant selection have also been developed in the electronic industry. Green et al. (2010) compared air, liquid, and phase-change cooling performance using FoMs that did not consider fluid mass [35].

A FoM which includes mass is critical in enabling favorable coolant selection for aerospace applications. It is apparent that none of the above-mentioned FOMs capture

Journal of Engineering for Gas Turbines and Power. Received July 03, 2024;
Accepted manuscript posted July 22, 2024. doi:10.1115/1.4066047

the effect of coolant mass and so a new FoM is developed here to assist in selecting coolants for high heat transfer, low pumping power, and low mass applications. Thermophysical properties and pipe flow equations are used to arrive at the FoM (denotated by ϕ) given in Equation (1) – the complete derivation is provided in Appendix A. The FoM maximizes the specific heat transfer rate ($\dot{Q}/\rho$) for a given pumping power (P_p). The FoM has units of (J/K)(m/kg$^{4/3}$). The index b does not affect the units as it arises from a correlation between dimensionless numbers.

$$\phi = \frac{c_p}{\left(\mu^{b/(3\text{-}b)}\right)\left(\rho^{(1\text{-}b)/(3\text{-}b)}\right)} = \frac{c_p}{\mu^{1/14}\rho^{2/7}} \qquad (1)$$

Blasius's correlation gives values of b = 1 and b = 0.2 for laminar and turbulent flow respectively [36]. A Reynolds number in the turbulent regime is expected in practice because of the high mass flow rates required for cooling. The FoM for turbulent flow is given in Equation (2).

$$\phi = \frac{c_p}{\mu^{1/14}\rho^{2/7}} \qquad (2)$$

To select a favorable coolant, ϕ must be maximized at the anticipated bulk operating temperature. By maximizing ϕ a coolant with a high heat transfer rate and low mass is selected for a given pumping power. Table 2 compares definitions of FoMs from wider literature with the newly proposed FoM from Equation (2). The new FoM captures heat transfer, pressure loss, and mass effects. None of the previous FoMs considered mass, which (as discussed above) is critical in aerospace applications.

Table 2: Comparison of proposed figure of merits.

Journal of Engineering for Gas Turbines and Power. Received July 03, 2024;
Accepted manuscript posted July 22, 2024. doi:10.1115/1.4066047

FoM	Maximize for…		Reference
	High	Low	
$\rho^{0.8}k^{0.6}{c_p}^{0.4}/(\mu^{0.4})$	$\bar{h}$	–	Mouromtseff [30]
$\rho^{2}{c_p}^{2.8}/(\mu^{0.2})$	$\dot{Q}$	P_p	Bonilla [31]
$\rho^{2}{c_p}^{1.6}k^{1.8}/(\mu^{1.4})$	$\dot{Q}$	P_p	Lenert *et al.* [32]
$\rho^{0.5}{c_p}^{0.5}k^{0.5}/(\mu^{0.25})$	$\dot{Q}$	P_p	Ehrenpreis *et al.* [33]
$c_p/\left(\mu^{1/14}\rho^{2/7}\right)$	$\dot{Q}/\rho$	P_p	Current study

A database of 43 coolants was constructed from the following references [20,21,37-40]. These coolants are classified as hydrocarbon (aromatic, aliphatic, and other HC), pure glycol, silicone, and aqueous. Figure 4 shows FoM regions for these

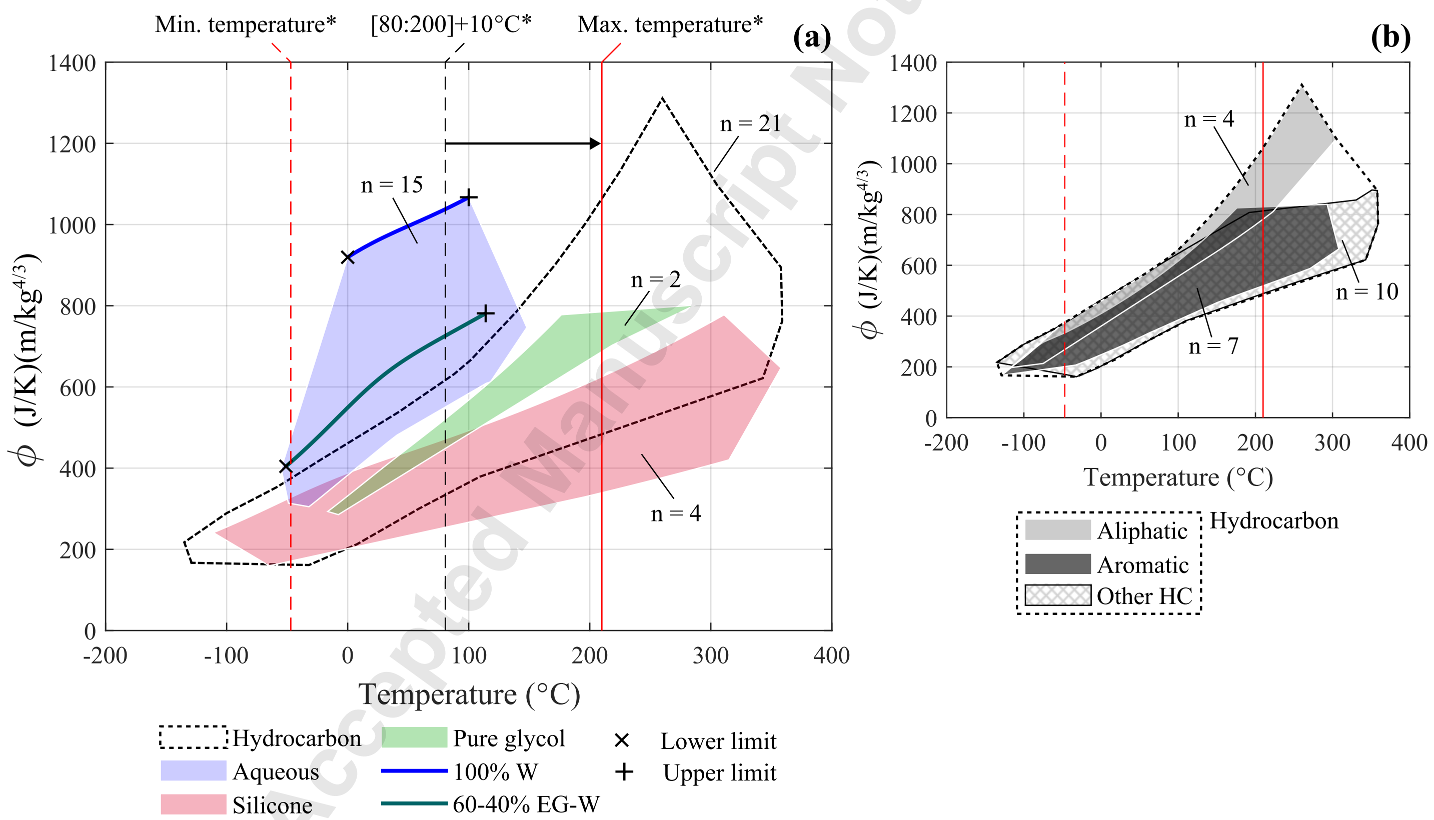

Figure 4: (a) Figure of Merit for coolant categories spanning their operating temperature at atmospheric pressure. The dashed line encompasses all of the Hydrocarbons. (b) Magnification of the Hydrocarbons which identifies Aliphatics, Aromatics, and Other HCs. *Refer to Table 1.

Journal of Engineering for Gas Turbines and Power. Received July 03, 2024;
Accepted manuscript posted July 22, 2024. doi:10.1115/1.4066047

coolant categories across their operating temperature at 1 bar; at higher pressure their boiling points increase. The minimum and maximum temperature lines align with those outlined in Table 1. Note that for clarity, the main plot in Figure 4(a) does not distinguish between hydrocarbon types (the hydrocarbon region is broken down into subregions in Figure 4(b)). As is the case for Ashby charts, Figure 4 is intended for broad comparisons required in preliminary design. The temperature spans the freezing point to boiling point for aqueous coolants, and the pour point to boiling point for other coolants. The freezing and pour points are lower limits, and the boiling point is the upper limit. The upper and lower limits form a region's boundary. The addition of more coolants increases confidence in the boundaries of each region – the number of coolants in each genus is denoted by n.

It is apparent from Figure 4 that aqueous coolants operating at 80-100°C outperform other coolant categories. Although the temperature range of water is extended by adding glycol, the FoM deteriorates as indicated by the difference between the curves for Water (W) and 60-40% Ethylene Glycol and Water (EG-W). Operating below -47°C is challenging with aqueous coolants. IT and HT-PEMFCs require use of hydrocarbons and silicones to avoid boiling if the coolant pressure is not increased above atmospheric pressure.

The average FoM and operating temperatures for coolant categories are compared statistically in Figures 5(a) and 5(b) respectively – note that pure glycol is not included as the n = 2 sample does not provide robust statistical outputs. $\overline{\phi}$ is the

Journal of Engineering for Gas Turbines and Power. Received July 03, 2024;
Accepted manuscript posted July 22, 2024. doi:10.1115/1.4066047

integrated average bounded by the lower and upper temperature limits for each coolant; the average FoMs are grouped for each genus to produce the statistics. Similarly, the temperature statistics are generated from the lower and upper temperature limits.

Aqueous coolants achieve the highest median average FoM of $\overline{\phi}$ = 691 (J/K)(m/kg$^{4/3}$). Aqueous coolants also have the largest interquartile range of $\overline{\phi}$. The large range is attributed to the large quantity of different aqueous coolant compositions. However, aqueous coolants have the smallest operating temperature range, which limits their suitability for IT and HT-PEMFCs. In addition, aliphatic coolants achieve a higher median $\overline{\phi}$ than other HCs, aromatics, and silicones which makes them more favorable in general. This performance difference is one of the reasons for the widespread adoption of polyalphaolefin (PAO) coolants (an aliphatic) in aircraft cooling installations [37].

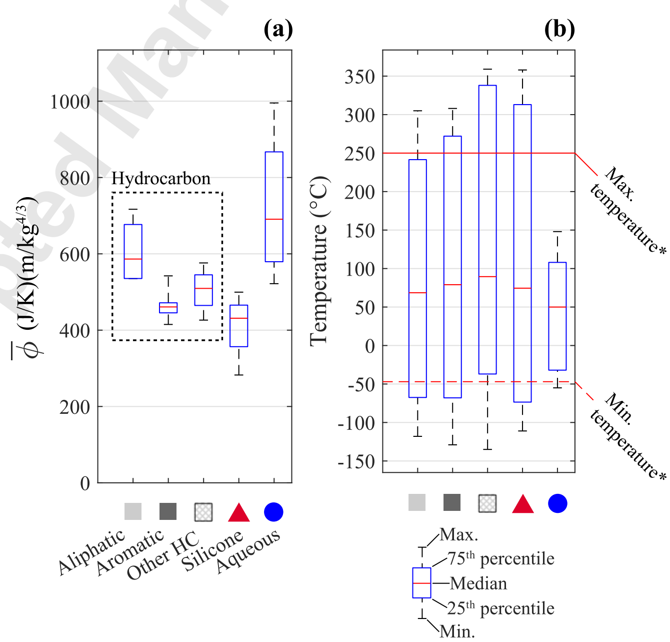

Journal of Engineering for Gas Turbines and Power. Received July 03, 2024;
Accepted manuscript posted July 22, 2024. doi:10.1115/1.4066047

Figure 5: (a) Integrated average Figure of Merit for coolant categories and (b) their operating temperature range. *Refer to Table 1.

4. SYSTEM MODEL

The FoM cannot capture system-level objectives, which limits its application to initial screening for suitable coolants. A system model is required for a higher fidelity selection. The process of choosing a suitable coolant differs between the FoM and the system model, with the distinctions outlined as follows:

1. The FoM maximizes the ratio of specific heat transfer rate ($\dot{Q}/\rho$) to the pumping power (P_p) for a given system – it is a metric based on the thermophysical properties of a coolant. Variables that define the condition of the system (mass flow rate, *etc*.) are constants in its derivation.
2. In the system model, the thermophysical properties are varied by changing the coolant. For a given heat transfer rate, the parasitic power and system mass are computed. Coolants are selected if they are "Pareto efficient" solutions.

These approaches achieve the same objective, they select coolants which maximize the heat transfer rate, and minimize the parasitic power and mass. The system model, principal assumptions, boundary conditions, and the sensitivity to relevant boundary conditions are addressed in the following sections.

4.1 Summary of the Model

The system model comprises a radiator, stack, piping, and pump, as illustrated in Figure 6(a). These are fundamental TMS components for liquid cooling and so ensure

Journal of Engineering for Gas Turbines and Power. Received July 03, 2024;
Accepted manuscript posted July 22, 2024. doi:10.1115/1.4066047

that the coolant selection procedure provides general recommendations. For a detailed review of different architectures and TMS components the interested reader is referred to [41]. The flow of data within the model and the key functions that it uses are outlined in Figure 6(b), with associated details provided below:

- Indicative boundary conditions for a PEMFC-powered aircraft were set – these are discussed in §4.4.

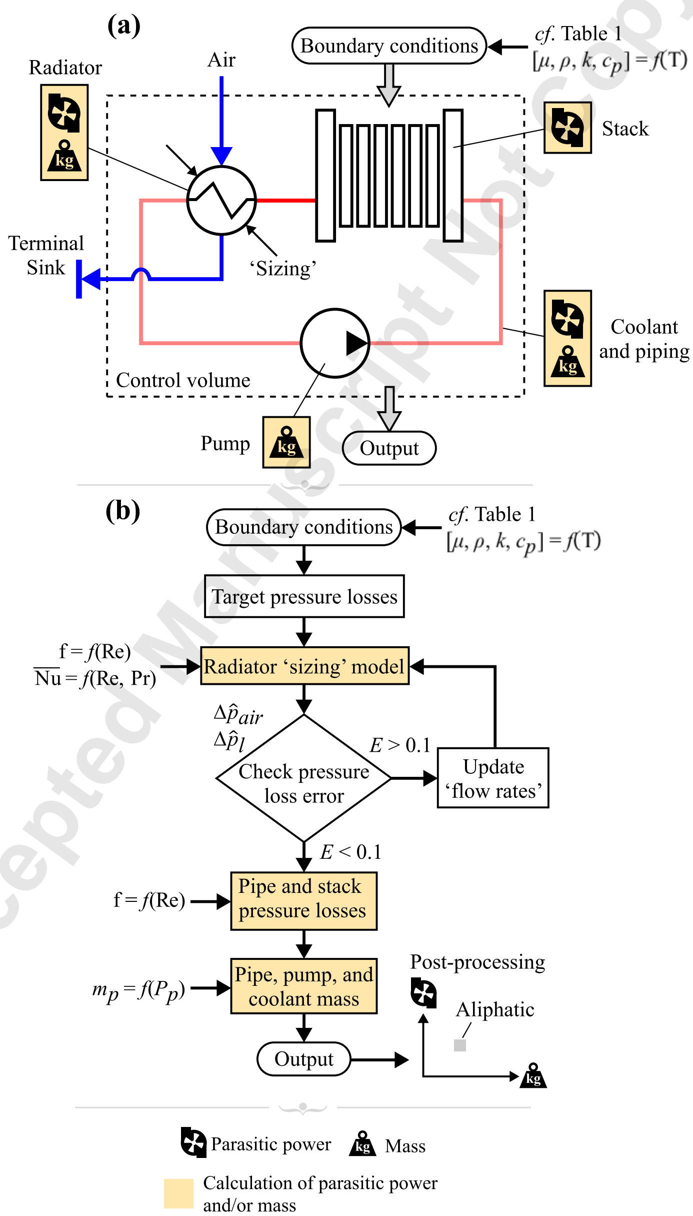

Journal of Engineering for Gas Turbines and Power. Received July 03, 2024;
Accepted manuscript posted July 22, 2024. doi:10.1115/1.4066047

Figure 6: (a) A schematic of the system model including the radiator, stack, piping, coolant and pump. (b) A flowchart of the system model which includes the iterative radiator sizing algorithm.

- A database was constructed from coolant suppliers. Coolant property data were curve fitted via regression. The coefficients of the fits were preloaded into the model to increase computation speed. Second order polynomials were employed for the density, thermal conductivity, and specific heat capacity. A two-term exponential was used for the dynamic viscosity. The R-squared is >0.95 for every coolant and fit. To define the operational temperature range of a coolant, the freezing, pour, and boiling points were taken from coolant suppliers. Air property data was linearly interpolated from Roger and Mayhew [42].
- The radiator sizing model was derived from London and Kays [43]. Although the heat exchanger characteristics affect the absolute 'size' of the radiator, they are unimportant in assessing the relative performance of the coolants. A crossflow heat exchanger composed of tubes with plate fins (11.32-0.737-SR) was used here [43]. To determine the radiator size, target pressure losses were assigned to both the air and coolant sides. An iterative algorithm was then utilized to achieve the set pressure loss targets. This process involved three stages:

  <u>Stage 1.</u> Initialization of the algorithm by assuming the mass flow rate flux was infinitesimal on both the air and coolant sides.

  <u>Stage 2.</u> Calculation of the friction factor for pressure loss, and the Colburn j-factor and the Nusselt number for heat transfer using empirical correlations

Journal of Engineering for Gas Turbines and Power. Received July 03, 2024;
Accepted manuscript posted July 22, 2024. doi:10.1115/1.4066047

suitable for both the air and coolant sides. On the airside, the friction factor and j-factor data from London and Kays for the 11.32-0.737-SR surface was used. On the coolant side, Churchill's Nusselt correlation was adopted to estimate the heat transfer coefficient in a smooth tube for 11.32-0.737-SR [44]. The friction factor for a circular tube was estimated from Haaland's explicit formula [36].

Stage 3. Estimation of the pressure loss on each side and recalculation of the new mass flow rate fluxes until the specified target pressure losses were reached. Note, entry and exit loss coefficients were derived from London and Kays. Linear interpolation was used to estimate these coefficients.

- A friction factor pipe flow correlation was used to estimate the pressure losses in the stack and piping from Haaland's explicit formula [36] using the calculated coolant mass flow rate from above. The pump mass was then estimated from an empirical correlation derived from [45]. A positive displacement coolant pump was assumed because they are used in fuel systems for aircraft. The correlation presented in Equation (3) includes an electric motor to drive the pump (units of kW and kg). The correlation for the electric motor mass was adopted from [46,47].

$$m_p = \underbrace{3.40 P_p^{\,0.437}}_{\text{pump}} + \underbrace{0.889 P_p^{\,0.900}}_{\text{motor}} \qquad (3)$$

- The system pumping power, drag, and mass were calculated. The drag was estimated from the airside pressure loss across the core [43]. The drag estimate did not account for the ramjet thrust generated by heat addition on the airside, a

Journal of Engineering for Gas Turbines and Power. Received July 03, 2024;
Accepted manuscript posted July 22, 2024. doi:10.1115/1.4066047

phenomenon frequently referred to as the Meredith effect [48]. Drela showed the ramjet thrust is proportional to the freestream Mach number and heat load; both are consistent for different coolants [49]. Different coolants were ranked against each other: coolants which performed favorably were selected and their properties were checked to identify whether they met the critical minimum and maximum temperature requirements. Pareto fronts were generated to assess the trade-off between different objectives, *e.g.* parasitic power and mass for a given heat load.

4.1 Principal Assumptions

The analysis was simplified by making the specific assumptions discussed below, most of which applied to the radiator sizing model.

Losses were evaluated in the heat exchanger core. The effect of installation drag was not assessed for simplicity. The dimensions of the core, and hence the packaging of the radiator, are affected by the choice of coolant. A greater core drag corresponds to a larger frontal area owing to the target pressure losses remaining constant between coolants. Any coolant which results in a heat exchanger with an increased core drag and consequently a larger frontal area would in practice also exhibit higher installation drag. Hence, the ranking of coolants would be unchanged if installation drag was accounted for. The minor losses, manifolding, entry, and exit losses are not accounted for in the stack and piping [50].

Journal of Engineering for Gas Turbines and Power. Received July 03, 2024;
Accepted manuscript posted July 22, 2024. doi:10.1115/1.4066047

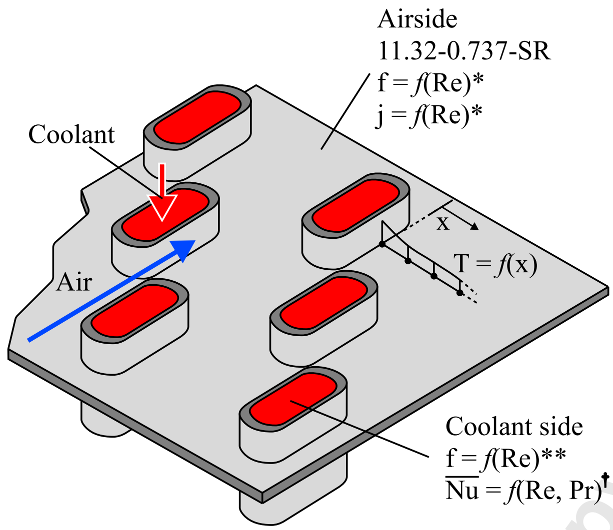

Figure 7: A schematic of radiator geometry (11.32-0.737-SR) with the respective correlations. *[43], **[36], and †[44].

Figure 7 shows a schematic of the 11.32-0.737-SR heat exchanger geometry adopted from London and Kays [43]. To simplify the analysis, circular tube correlations were used as an approximation for the flat tubes, and the internal flow was assumed to be fully developed. The friction factor and Colburn j-factor data from London and Kays were curve fitted with two-term exponentials. A two-term exponential was chosen for its ability to yield a lower Root Mean Squared Error (RMSE) in comparison to more conventional power laws. London and Kays quote the uncertainty as a nominal ±5% for this data. The fitted curves for 11.32-0.737-SR had a R-squared >0.95. London and Kays included three rows in the test article used to produce the correlations for 11.32-0.737-SR. The number of rows affects the prediction of heat transfer and pressure loss, with Zukauskas suggesting that 16 rows are required before the average heat transfer coefficient settles [51]. Hence, the model's prediction of a heat exchanger with more than the three rows used to generate the correlations introduces uncertainty. It should

Journal of Engineering for Gas Turbines and Power. Received July 03, 2024;
Accepted manuscript posted July 22, 2024. doi:10.1115/1.4066047

be noted that the model allows a non-integer number of tube rows as an output. This enables minor variations in radiator mass to be captured during coolant ranking, *i.e.* it increases the sensitivity of the analysis. This approach allows a TMS designer to select an appropriate coolant for their application and then proceed to refine the design of the radiator (the 11.32-0.737-SR geometry used here was chosen as baseline – there are many geometries that could be chosen from, and scaling up to the nearest integer of rows for the analysis could lead to sub-optimal coolant selection).

4.3 Boundary Conditions for Coolant Selection

The boundary conditions used in this study are summarized in Table 3, with associated sensitivities addressed in §4.4. The values are indicative of those for an aircraft operating with a liquid cooled PEMFC powertrain capable of delivering a maximum electrical power of 1 MW. It was assumed that a single stack produced $\dot{W}_1$ = 100kW [52]; the powertrain thereby comprised ten stacks to generate the required power. For assumed cell efficiencies of 50%, the total rate of heat generated by the powertrain at maximum power was $\dot{Q}$ = 1 MW [53]. The stack geometry was derived from data given by PowerCell, Bargal *et al.*, and Yoshida *et al.* [52,54,55]. Each stack comprised 240 cells of pitch p = 2.5 mm, providing a stack length of L_s= 0.6 m. Cooling channels inside stacks typically have hydraulic diameters of around a millimeter and undergo multiple passes [56] – here b_s = 1 mm and N = 20 were used as representative values.

Conventional aircraft commonly employ aluminum pipework and radiators [57-59]. As such, material properties for aluminum (ρ_m = 2800 kg/m^{3}and k_m = 187 W/mK)

Journal of Engineering for Gas Turbines and Power. Received July 03, 2024;
Accepted manuscript posted July 22, 2024. doi:10.1115/1.4066047

were used [36,51]. Ions leaching from aluminum into the coolant pose challenges in fuel cells, which would in practice necessitate the use of deionizers to prevent short-circuiting [60] – the effect of deionizers on thermal performance was not considered here. Representative dimensions for the inlet duct (intake area A_{in} = 0.5 m^2) and piping (hydraulic diameter D_h = 100 mm, wall thickness t = 10mm, surface roughness ε = 0.046 mm and length L_p = 5 m) were informed by preliminary design studies.

The radiator was sized for take-off (altitude h = 0 ft), representing the most demanding performance requirement. At this point, the air-to-coolant temperature difference and Mach number (M_∞ = 0.2) are at their minimum, while the heat load is at its 1 MW maximum. This ensures that the selected coolant is suitable for the entire mission profile. To evaluate the worst-case scenario, the International Standard Atmosphere (ISA) was employed, with the ambient temperature increased by δT = 25°C to represent a hot day [61]. The diffuser adiabatic efficiency was taken as η_d = 0.9 – this is typical of well-designed diffusers [62]. The coolant inlet temperature ($T_{l_{in}}$) was obtained from the stack operating temperature. This temperature depends on the fuel cell MEA, as discussed in §1. A range of 80-200°C is employed here because the TRL of stacks operating >200°C is low. Minimizing the non-uniformity of the MEA surface temperature is crucial to prevent elevated degradation rates [54,63]. The temperature difference on the coolant-side is taken as ΔT_l = 20°C to limit this temperature gradient. The coolant-side is assigned a target pressure loss of $\Delta\hat{p}_l$ = 0.5 bar across the radiator. While this target is contingent on the design of the system, Topuz *et al.* demonstrated similar pressure losses for a liquid-cooled radiator loop [64]. An allowable pressure loss

Journal of Engineering for Gas Turbines and Power. Received July 03, 2024;
Accepted manuscript posted July 22, 2024. doi:10.1115/1.4066047

coefficient is implemented on the airside. This parameter defines the target pressure loss on the airside as a fraction of the available dynamic pressure; a value of greater than one corresponds to an airside pressure loss greater than the dynamic pressure. A baseline value of ξ = 0.5 is adopted to ensure that the total pressure aft of the radiator is maintained above ambient.

Table 3: System model boundary conditions for coolant selection.

Parameter	Magnitude	Unit
$\dot{W}_1$	100	kW
$\dot{Q}$	1	MW
p	2.5	mm
L_s	0.6	m
b_s	1	mm
N	20	-
ρ_m	2800	kg/m^3
k_m	187	W/mK
A_{in}	0.5	m^2
D_h	100	mm
t	10	mm
ε	0.046	mm
L_p	5	m
h	0	ft
ΔT_l	20	°C
M_∞	0.2	-
δT	25	°C
η_d	0.9	-
$T_{l_{in}}$	80:200	°C
$\Delta\hat{p}_l$	0.5	bar
ξ	0.5	-

4.4 Sensitivity to Boundary Conditions

The following sensitivity analysis shows that the coolant inlet temperature is the boundary condition that provides the largest contribution to total mass (M_t – piping,

Journal of Engineering for Gas Turbines and Power. Received July 03, 2024;
Accepted manuscript posted July 22, 2024. doi:10.1115/1.4066047

coolant, and dry radiator core mass) and total power (P_t – pumping power and core drag). Sensitivity was captured from a full factorial Design of Experiments (DoE) with two levels ('low' and 'high') applied to the boundary conditions presented in Table 4 (see references [65,66] for a discussion of the associated DoE methodology). All other boundary conditions remained at the nominal values provided in Table 3. The boundary conditions in Table 4 were considered at two-levels as they are the most uncertain based on preliminary designs and trade studies. By showing that the coolant inlet temperature is the most important boundary condition, the number of degrees of freedom is reduced in subsequent analysis and coolant selection is generalized.

Table 4: Full factorial Design of Experiments with two levels to determine the sensitivity of total mass and total power to uncertain boundary conditions.

Parameter	Low	High	Unit
A_{in}	0.4	0.6	m^2
$T_{l_{in}}$	80	200	°C
ΔT_l	20	30	°C
$\Delta\hat{p}_l$	0.5	0.8	bar
ξ	0.5	0.8	–

The percentage contributions of each main effect and their interactions on the response variables M_t and P_t are shown in Figure 8 for aliphatic coolant YF-22 PAO (interacting variables are denoted with a colon). The percentage contributions were estimated from the sum of the squares; it provides a measure of the contribution of the main effects and interactions relative to the total sum of squares. Hence, a larger contribution signifies a model term (main effect or interaction) which has a greater relative importance on the response variable.

Journal of Engineering for Gas Turbines and Power. Received July 03, 2024;
Accepted manuscript posted July 22, 2024. doi:10.1115/1.4066047

Figure 8(a) shows the percentage contribution of the model terms on the total mass. The coolant inlet temperature (highlighted in Table 4) is the most significant model term, accounting for ~50% of the contribution to mass. Figure 8(b) shows the percent contribution on the pumping and core drag power. The coolant inlet temperature accounts for ~70% of contribution to total power. The coolant inlet temperature had the largest contribution of any of the boundary conditions considered in the DoE. Changing the boundary conditions for a fixed coolant inlet temperature will lead to a similar coolant being selected because the other boundary conditions have a minor influence on the mass and power. This enhances the general applicability of the results, allowing the selection of favorable coolants by adjusting the inlet coolant temperature only. The understanding that other boundary conditions exert only a minor influence on the selection process adds robustness to the coolant selection approach.

Figure 8 was generated for YF-22 PAO (aliphatic) because it has a high boiling point (>200°C), which allowed contributions to total mass and power to be considered over the full range of $T_{l_{in}}$. Although the contributions do vary for different coolants, the coolant inlet temperature remains the most important. To avoid boiling when comparing the contributions of different coolants, 120°C was used as the high value of the coolant inlet temperature instead of 200°C. Each coolant genus was sampled once with this high value, the minimum contribution to both total mass and power attributed to the coolant inlet temperature was ~30% (a silicone coolant) and the average was ~70%.

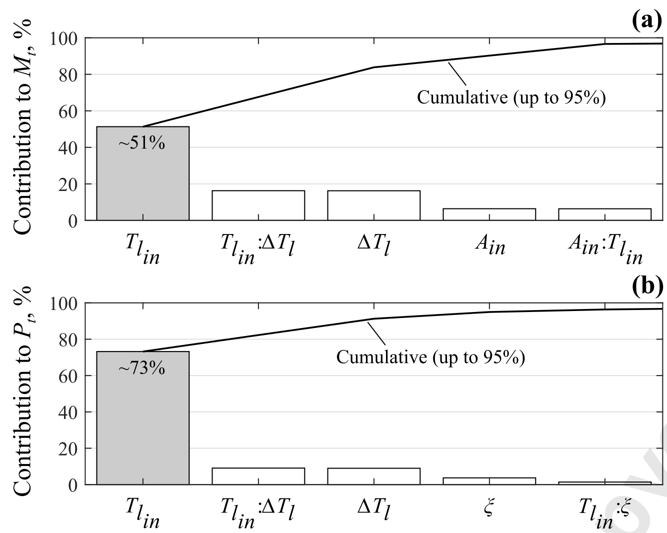

Figure 8: Percent contribution of the model terms on (a) total mass and (b) total power. derived from a full factorial Design of Experiment for an Aliphatic coolant. Up to 95% of the percent contribution is included.

5. SELECTION OF A LIQUID COOLANT

The maximum and minimum operating temperatures and electrical conductivity requirements for coolants operating on PEMFC-powered aircraft were provided in Table 1. Maximum temperature was applied as a constraint in the selection process used to produce the results shown in Figures 9 and 10. The minimum temperature constraint is specific to aircraft requirements and often operational mitigations can be made. As such, minimum temperature constraints are addressed subsequently in §5.3. Mitigations include the use of electrical heaters, and the design of a freeze tolerant system. Electrical conductivity is also discussed in §5.3. Inhibitors can be introduced to the coolant to reduce the conductivity, and deionizers can be integrated into the system.

Journal of Engineering for Gas Turbines and Power. Received July 03, 2024;
Accepted manuscript posted July 22, 2024. doi:10.1115/1.4066047

Figure 9(a) shows normalized total power ($\tilde{P}_t$ – pumping power *and* core drag) versus the normalized total mass ($\widetilde{M}_t$) at 80°C, and Figure 9(b) shows normalized pumping power ($\tilde{P}_p$) versus the normalized total mass at 80°C. The data is normalized by deionized water at 80°C. Figure 9(a) aids in the selection of favorable coolants for aircraft radiators where freestream velocities are high and drag is important; Figure 9(b) is relevant when the freestream velocity is relatively low and core drag is not important (*e.g.* automotive and marine applications) – these "use cases" are addressed in Table 5. To select a favorable coolant, the powers and mass must be minimized. The most favorable coolant for both Figures 9(a) and 9(b) is deionized water. This coolant is Pareto efficient because it achieves a dominance rank of one. Aqueous coolants perform better than other coolants at 80°C. There are two aromatic outliers, and one other hydrocarbon outlier; these show better performance than most hydrocarbon coolants. This indicates that the composition of hydrocarbon coolants can be tailored to achieve similar performance to aqueous coolants at 80°C if required. Pure glycols show worse performance to aqueous coolants, yet they perform better than most hydrocarbon and silicone coolants.

Journal of Engineering for Gas Turbines and Power. Received July 03, 2024;
Accepted manuscript posted July 22, 2024. doi:10.1115/1.4066047

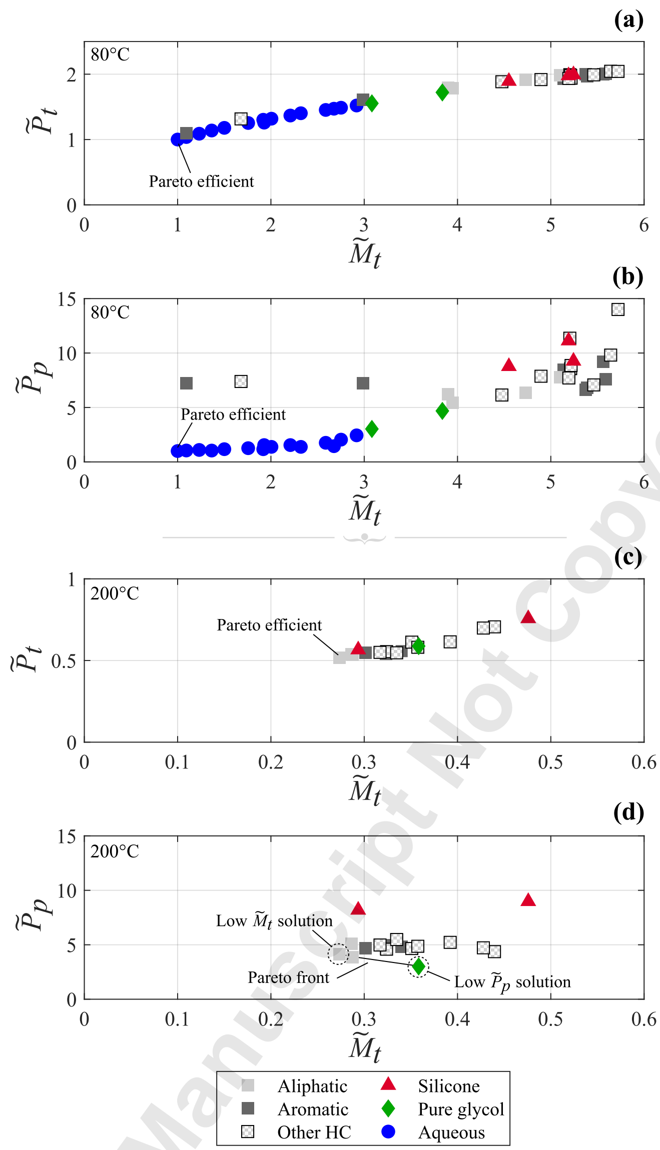

Figure 9: Pareto fronts at 80°C for (a) and (b), and 200°C for (c) and (d). Total power versus total mass: (a) and (c). Pumping power versus total mass: (b) and (d). Normalized by deionized water at 80°C. Excludes low temperature threshold.

Figure 9(c) shows $\tilde{P}_t$ versus $\widetilde{M}_t$ at 200°C, and Figure 9(d) shows $\tilde{P}_p$ versus $\widetilde{M}_t$ at 200°C. In both figures aqueous coolants are not plotted because they boil below 200°C, which makes them unsuitable for selection. Figure 9(c) shows that aliphatic coolants are Pareto efficient. In Figure 9(d), both aliphatic coolants and a pure glycol form a Pareto

Journal of Engineering for Gas Turbines and Power. Received July 03, 2024;
Accepted manuscript posted July 22, 2024. doi:10.1115/1.4066047

front (this is formed when more than one coolant is Pareto efficient). The low $\tilde{P}_p$ and low $\widetilde{M}_t$ solutions are circled on the Pareto front. In Figures 9(c) and 9(d) the range in normalized total mass is 0.27 to 0.47. This is smaller than the range in Figures 9(a) and 9(b). Hence, the performance difference between coolant compositions is smaller at 200°C compared to 80°C.

5.1 Selection with Core Drag

The full factorial DoE in §4.4 revealed that the coolant inlet temperature (a proxy for the stack temperature) was the parameter with the strongest effect on the total mass and power of the TMS. The model was thereby employed to generate data using coolant inlet temperatures in the range 80-200°C with all other parameters set to the values provided in Table 3. The Pareto efficient coolant(s) were selected for each temperature via dominance ranking.

Figures 10(a) and 10(b) show $\tilde{P}_t$ versus $\widetilde{M}_t$ for the Pareto efficient coolants. Data points were generated at 10°C coolant inlet temperature intervals (these temperatures are labelled on the plots). Pareto fronts are illustrated by a single line connecting coolants from the low $\tilde{P}_t$ to low $\widetilde{M}_t$ solutions (*cf*. 160°C, 170°C and 180°C in Figure 10(b)). Pareto efficient solutions in between the low $\tilde{P}_t$ and low $\widetilde{M}_t$ solutions are omitted to aid visual interpretation. Four significant trends are observed:

1. Between 80 and 110°C there is a ~50% reduction in $\widetilde{M}_t$ and a ~30% reduction in $\tilde{P}_t$. This highlights the benefit of using higher-temperature PEMFCs. Note, the percentage reduction in $\tilde{P}_t$ and $\widetilde{M}_t$ reduces as the temperature increases.

Journal of Engineering for Gas Turbines and Power. Received July 03, 2024;
Accepted manuscript posted July 22, 2024. doi:10.1115/1.4066047

2. Aqueous coolants are favorable for LT-PEMFCs operating in the range 80-90°C, but are not optimal for PEMFCs operating at temperatures above 90°C for two reasons:
   - First, they have relatively low boiling points. At elevated temperatures aqueous coolant loops must be pressurized to prevent boiling; this poses challenges for the design of high burst pressure coolant channels and seals within the stack.
   - Second, cooling systems operating with aqueous coolants need (as predicted by the model) radiators with relatively large frontal areas. This increases core drag and thus $\tilde{P}_t$.
3. Aromatic coolants are suited to IT-PEMFCs (100-120°C).
4. Aliphatic coolants are favorable at HT-PEMFC (120-200°C) operating temperatures.

Journal of Engineering for Gas Turbines and Power. Received July 03, 2024;
Accepted manuscript posted July 22, 2024. doi:10.1115/1.4066047

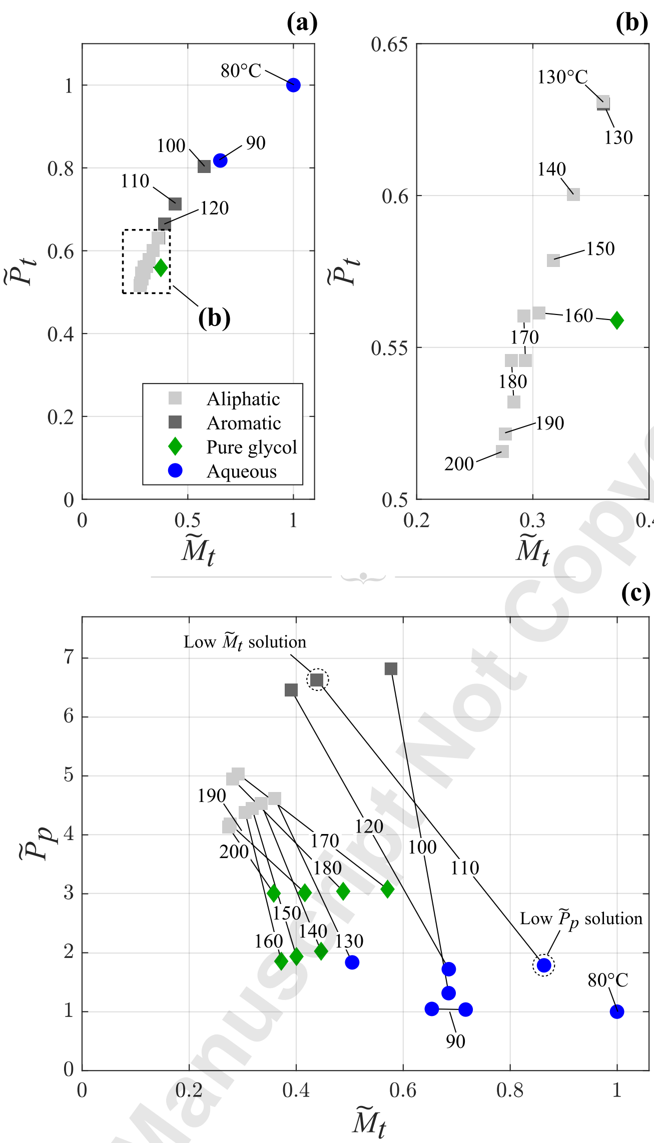

Figure 10: Pareto efficient coolants for 80–200°C. (a) Normalized total power versus Normalized total mass. (b) Magnification of (a). (c) Normalized pumping power versus Normalized total mass. The number labels correspond to the operating temperature.

5.2 Selection without Core Drag

Figure 10(c) shows $\widetilde{P}_p$ versus $\widetilde{M}_t$ for the Pareto efficient coolants. It is evident from comparison of Figures 10(a) and 10(c) that core drag has a significant impact on the selection of favorable coolants. The trend in Figure 10(c) aligns with the prevalent

Journal of Engineering for Gas Turbines and Power. Received July 03, 2024;
Accepted manuscript posted July 22, 2024. doi:10.1115/1.4066047

use of glycol and aqueous coolants in the automotive industry where the freestream velocity (core drag) is small compared to aircraft and the mass is less critical. Note, the low $\tilde{P}_p$ to low $\widetilde{M}_t$ solutions are circled for 110°C with the connecting line signifying the Pareto front. Three significant trends are observed:

1. There is an overall reduction in total mass as the operating temperature increases from 80-200°C. The temperature difference driving the heat transfer between the coolant and ambient air increases as the operating temperature increases – this reduces the required heat transfer surface area in the radiator for a given heat load, i.e. a smaller (and thus lower mass) radiator can be used in the TMS. It is important to note that the trend is not monotonic. For instance, the total mass increases from 100-110°C for aqueous coolants, and from 160-170°C for pure glycol. This is due to changes in coolant composition to satisfy the boiling margin. If the PEMFC operating temperature exceeds the boiling point of a coolant, then that coolant can no longer be considered for selection – this means that a coolant that was deemed sub-optimal at a lower operating temperature may become pareto efficient at a higher operating temperature.
2. Aqueous coolants begin to boil beyond 130°C. The low $\tilde{P}_p$ Pareto efficient solutions switch from aqueous coolants to pure glycols accordingly.
3. The Pareto fronts result in a trade-off between $\tilde{P}_p$ and $\widetilde{M}_t$. Aromatic and aliphatic coolants generally result in higher pumping powers and lower total masses compared with aqueous solutions and pure glycols at a specific temperature. For example, at 170°C, $\tilde{P}_p$ = 5.0 and $\widetilde{M}_t$ = 0.29 for the Pareto efficient aliphatic, and $\tilde{P}_p$ =

3.1 and $\widetilde{M}_t$ = 0.57 for the Pareto efficient pure glycol – as such the aliphatic would be selected for a low mass use case and the glycol would be selected for a low pumping power use case.

5.3 Selection with Core Drag – with the Minimum Temperature and Electrical Conductivity Thresholds

The minimum temperature constraint from Table 1 was applied to the results in Figures 10(a) and 10(b) to generate Figures 11(a) and 11(b). It is apparent that aqueous and pure glycol solutions are no longer viable – this suggests that hydrocarbon-based coolants are the most suitable for aircraft at a coolant pressure of 1 bar (pressurizing the coolant loop can raise the boiling point of aqueous solutions, but this approach is not considered in this study). Aromatics show favorable performance between 80-130°C while aliphatics outperform them between 130-200°C. Improvements in performance are shown to diminish at elevated temperature and so coolant selection is more important for aircraft powered by LT and IT-PEMFCs than those powered by HT-PEMFCs. Further improvements in system-level performance must come from other developments in the TMS beyond coolant selection and elevated temperatures.

Mohapatra and Loiskits report that the electrical conductivity of aromatics and aliphatics is negligible due to their dielectric properties [19]. In contrast, aqueous solutions necessitate the use of inhibitors and deionizers to control electrical conductivity. Hence, the aromatics and aliphatics outlined in Figure 11 also satisfy the electrical conductivity threshold (*cf*. Table 1).

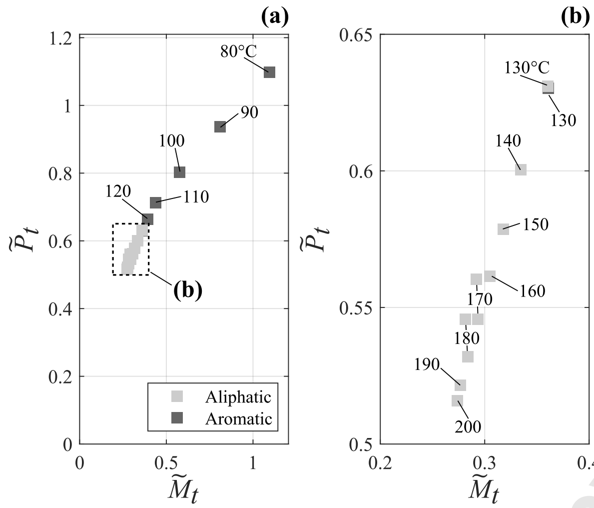

Figure 11: Pareto efficient coolants for 80–200°C. (a) Normalized total power versus Normalized total mass. (b) Magnification of (a). The number labels correspond to the operating temperature.

5.4 Use Cases for Coolant Selection

Table 5 outlines several practical cases pertinent to coolant selection for liquid cooled PEMFC applications – the requirements from Table 1 are applied. Case I is the most relevant to aircraft; Cases II and III are relevant to applications where minimizing radiator core drag is not an essential TMS requirement. Applying the methodology developed in this paper to different use cases demonstrates its versatility.

Table 5: Liquid coolant use cases.

Case	Delineation
I	Aerospace: typified by low mass and low parasitic power. Pareto efficient coolants that minimize $\widetilde{P}_t$ and $\widetilde{M}_t$.
II	Automotive: where low mass is prioritized over low pumping power.

Journal of Engineering for Gas Turbines and Power. Received July 03, 2024;
Accepted manuscript posted July 22, 2024. doi:10.1115/1.4066047

	Low $\widetilde{M}_t$ solutions on the Pareto front that minimize $\tilde{P}_p$ and $\widetilde{M}_t$.
III	<u>Marine:</u> where low pumping power is prioritized over low mass. Low $\tilde{P}_p$ solutions on the Pareto fronts that minimize $\tilde{P}_p$ and $\widetilde{M}_t$.

In §3 the FoM (ϕ) was introduced for expedient screening of coolants. The screening technique involves selecting a coolant by maximizing ϕ at a given operating temperature. Figure 12 plots the maximized ϕ against temperature (the max(ϕ) curve). Equation (1) was used to calculate ϕ for the Pareto efficient coolants for the cases described in Table 5 – these are plotted on Figure 12 for comparative purposes. Cases I and II show agreement with the max(ϕ) for >110°C and Case III shows agreement with the max(ϕ) for <150°C. Regions where there is a lack of agreement between the max(ϕ) curve and the curves for Cases I to III result from the difference in approach to generating the data used to plot the curves – data for the three use cases are obtained from the model, which captures system-level objectives, whereas data for the max(ϕ) curve is obtained from coolant properties alone (see discussion in §4). While the max(ϕ) curve is useful for screening purposes in preliminary TMS design, the *model* is recommended for higher fidelity selection because it uses the Pareto efficient solutions for the relevant case. For example, at 80°C the Pareto efficient coolant for Case I achieves a 53% decrease in $\widetilde{M}_t$ and a 22% decrease in $\tilde{P}_t$ compared to the coolant predicted by max(ϕ) – selecting a coolant with max(ϕ) alone would result in sub-optimal performance.

The modeling approach presented in this paper may not be practical where expedient coolant selection is required. In such scenarios, a TMS designer could use the curve from Figure 12 for the case that is most pertinent to their application. The coolant being considered is suitable for the application if ϕ matches the pertinent case at a given temperature (note: the coolant would also have to meet other system specific considerations, such as those in Table 1 for a PEMFC-powered aircraft). It is important to recognize that this approach may not necessarily yield the optimal coolant.

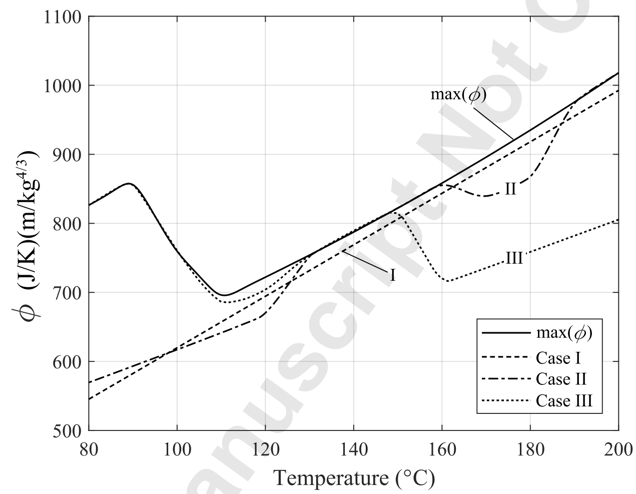

Figure 12: Cases for selecting suitable coolants. The requirements from Table 1 are applied.

6. CONCLUSION

Two approaches to selection of liquid coolants for Proton Exchange Membrane Fuel Cell (PEMFC) powered aircraft were considered for PEMFCs with operational temperatures in the range 80-200°C. The first approach maximized a Figure of Merit (FoM); the second approach relied on output of Pareto efficient solutions from a physically informed model of the Thermal Management System (TMS). The results from both approaches showed that coolant selection is highly sensitive to the PEMFC stack temperature. The outputs from the model indicated that there is a trade-off between mass and parasitic power of the TMS, and that TMS performance improves at elevated temperatures. The FoM provides a useful method for expediently screening coolants, but the *model* is recommended for optimal coolant selection.

The outputs from the model provided two key findings pertinent to PEMFC-powered aircraft:

1. It was shown for the case study presented here (a hybrid-electric aircraft using a 1MW PEMFC stack) that hydrocarbon-based coolants are favorable, with aromatics optimal for coolant inlet temperatures <130°C and aliphatics optimal for coolant inlet temperatures >130°C.
2. There are diminishing gains in performance at elevated temperatures. As such, a step change in system-level performance must come from developments other than coolant selection and increases in operating temperatures.

ACKNOWLEDGMENT

The authors would like to thank GKN Aerospace for their financial support and expertise, and Matthias Schröder (DLR) for providing the heat exchanger sizing data that enabled a comparison between models in Appendix B.

The datasets generated and supporting the findings of this article are obtainable from the corresponding author upon reasonable request.

APPENDIX A: FIGURE OF MERIT DERIVATION

Firstly, consider the heat transfer rate given in Equation (4); fluid properties are expressed as a separate grouping.

$$\dot{Q} = c_p \rho \cdot Q \Delta T \qquad (4)$$

The fluid properties depend on the coolant however the flow rate and temperature difference are constant. Equation (5) shows the Darcy-Weisbach equation, it is used to evaluate the pumping power.

$$\Delta p / L_p = \mathrm{f} \frac{\rho}{2} \frac{V^2}{D_h} \qquad (5)$$

The friction factor for fully developed turbulent pipe flow can be expressed as a function of Reynolds number; the form of Blasius's power law approximation is adopted in Equation (6) [36].

$$\mathrm{f} = C / \mathrm{Re}^b \qquad (6)$$

Equation (7) relates the pressure loss and friction factor to the pumping power by substituting (5) and (6).

$$P_p = \left(\frac{C A^{b-2} L_p}{2 {D_h}^{b+1}} \right) \cdot \rho^{1-b} \mu^b \cdot Q^{3-b} \qquad (7)$$

The flow rate in (7) is substituted with (4) to form Equation (8). To select coolants with a low mass, the specific heat transfer rate is adopted; this is analogous to specific strength in material selection. A high specific heat transfer rate corresponds to a high heat transfer rate and low mass.

Journal of Engineering for Gas Turbines and Power. Received July 03, 2024; Accepted manuscript posted July 22, 2024. doi:10.1115/1.4066047

$$P_p \propto \left(\frac{\dot{Q}}{\rho}\right)^{3\text{-}b} \frac{\rho^{1\text{-}b}\mu^b}{{c_p}^{3\text{-}b}} \qquad (8)$$

By manipulating the heat transfer rate with the density of the coolant, the effect of coolant mass is captured. The FoM (denotated by ϕ) is now derived by maximizing the specific heat transfer rate ($\dot{Q}/\rho$) for a given pumping power – refer to Equation (9).

$$\phi = \frac{c_p}{\mu^{\left({b}/{3\text{-}b}\right)}\rho^{\left({1\text{-}b}/{3\text{-}b}\right)}} \propto \frac{\dot{Q}}{\rho}\left(\frac{1}{P_p}\right)^{1/3\text{-}b} \qquad (9)$$

For laminar and turbulent flow, b = 1 and b = 0.2 [36]. The ϕ for a turbulent regime is given in Equation 10. As the friction factor is dimensionless the index b does not affect the units of the FoM. It has units of (J/K)(m/kg$^{4/3}$).

$$\phi = \frac{c_p}{\mu^{1/14}\rho^{2/7}} \qquad (10)$$

APPENDIX A: COMPARISON OF RADIATOR SIZING MODELS

Industry seldomly releases data pertaining to radiator mass. To aid comparison in the wider literature, the dry radiator core mass predicted by this model is released and it is compared to one developed independently by Schröder *et al*. [67]. A close agreement between these models is not expected given the large uncertainty in the correlations, and the differences in the construction of the models. Nevertheless, the trend is consistent; the dry heat exchanger core mass diminishes monotonically as the inlet coolant temperature increases.

Journal of Engineering for Gas Turbines and Power. Received July 03, 2024;
Accepted manuscript posted July 22, 2024. doi:10.1115/1.4066047

Schröder *et al*. employed a crossflow plate-fin heat exchanger with louvered fins and was validated at a single coolant inlet temperature with data from a manufacturer. Louvered fins are used on the airside; the coolant side has no secondary surface and tubes are employed [68,69]. The heat exchanger model proposed in this study is compared to Schröder *et al*. at coolant inlet temperatures from 70-98°C. The boundary conditions used to compare the models are given in Table 6.

Figure 13 illustrates the comparison between the models based on the dry radiator core mass using 50-50% EG-W as the coolant. On the airside, louvered fin correlations were employed from London and Kays (3/8-6.06). Note, Schröder *et al*. implemented louvered fin correlations from Chang *et al.* [43,68,69]. On the coolant side, heat transfer and friction factor correlations for tubes were utilized [36,44,70]. Each model relies on different correlations and coolant thermophysical property data. The comparison presented in Figure 13 does not amount to a validation because of these differences. Both models show consistent trends, the ranking of coolants should therefore be reliable between models.

Table 6: Boundary conditions used for both the radiator sizing models.

Parameter	Magnitude	Unit
$T_{air_{in}}$	35	°C
$T_{air_{out}}$	50	°C
ΔT_l	10	°C
$p_{air_{in}}$	1	bar
$\Delta \hat{p}_{air}$	0.05	bar
$\Delta \hat{p}_l$	0.1	bar
$\dot{Q}$	400	kW

Journal of Engineering for Gas Turbines and Power. Received July 03, 2024;
Accepted manuscript posted July 22, 2024. doi:10.1115/1.4066047

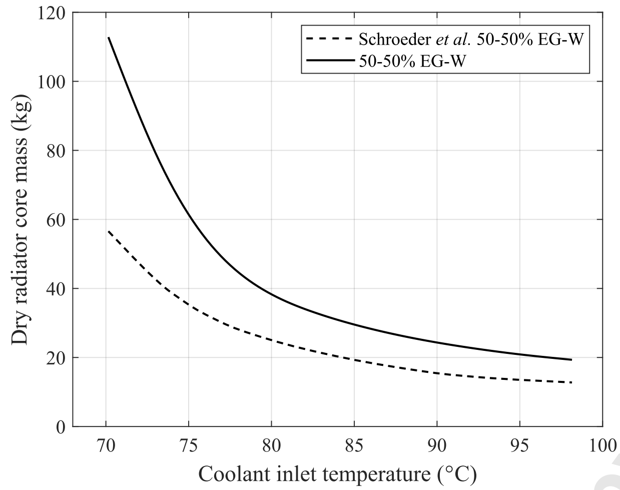

Figure 13: Comparison of the radiator sizing model with 50-50% EG-W to [67]. Dry radiator core mass versus coolant inlet temperature.

NOMENCLATURE

A	Flow area [m^2]
A_{in}	Duct intake area [m^2]
b	Empirical constant
b_s	Stack cooling channel width [m]
C	Empirical constant
c_p	Coolant specific heat capacity [J/kgK]
D_h	Hydraulic diameter [m]
E	Convergence error
f	Friction factor

Journal of Engineering for Gas Turbines and Power. Received July 03, 2024;
Accepted manuscript posted July 22, 2024. doi:10.1115/1.4066047

h	Altitude [ft]
$\bar{h}$	Convective heat transfer coefficient [W/m^{2}K]
j	Colburn j-factor
k	Coolant thermal conductivity [W/mK]
k_m	Radiator thermal conductivity [W/mK]
L_p	Pipe length [m]
L_s	Stack length (along the coolant axis) [m]
m_p	Pump mass [kg]
M_∞	Freestream Mach number
M_t	Total mass (coolant inside the radiator and pipes, dry radiator core, dry pump, and dry pipe mass) [m]
$\widetilde{M}_t$	Normalized total mass*
$\overline{Nu}$	Nusselt number
N	Number of coolant passes in a bipolar plate
p	Fuel cell pitch (distance between bipolar plates) [m]
$p_{air_{in}}$	Air inlet pressure [Pa]
P_p	Pumping power [W]
P_t	Total power (pumping and core drag power) [W]
$\tilde{P}_p$	Normalized pumping power*

$\tilde{P}_t$	Normalized pumping and core drag power*
Pr	Prandtl Number
Q	Volume flow rate [m^3/s]
$\dot{Q}$	Heat transfer rate [W]
Re	Reynolds number
t	Pipe wall thickness [m]
T	Temperature [°C]
$T_{air_{in}}$	Air inlet temperature [°C]
$T_{air_{out}}$	Air outlet temperature [°C]
$T_{l_{in}}$	Coolant inlet temperature [°C]
V	Bulk velocity [m/s]
$\dot{W}_1$	Power of a single stack [W]
x	Direction axis
δT	International Standard Atmosphere (ISA) temperature deviation (+25°C for hot day) [°C]
Δp	Pressure loss [Pa]
$\Delta\hat{p}_{air}$	Airside pressure loss target [Pa]
$\Delta\hat{p}_l$	Coolant side pressure loss target [Pa]
ΔT	Temperature difference [°C]

ΔT_l	Liquid coolant temperature difference [°C]
ε	Roughness [m]
η_d	Adiabatic diffuser efficiency
ξ	Allowable pressure loss coefficient
μ	Coolant dynamic viscosity [kg/ms]
ρ	Coolant density [kg/m^3]
ρ_m	Pipe and radiator density [kg/m^3]
ϕ	Figure of Merit (FoM) [(J/K)(m/kg$^{4/3}$)]
$\overline{\phi}$	Average Figure of Merit (FoM) [(J/K)(m/kg$^{4/3}$)]

Journal of Engineering for Gas Turbines and Power. Received July 03, 2024;
Accepted manuscript posted July 22, 2024. doi:10.1115/1.4066047

REFERENCES

[1] International Air Transport Association (IATA), 2021, "Net-Zero Carbon Emissions by 2050," International Air Transport Association (IATA), accessed Dec. 15, 2023. https://www.iata.org/en/pressroom/pressroom-archive/2021-releases/2021-10-04-03/.

[2] Raillant-Clark, W., 2022, "States adopt net-zero 2050 global aspirational goal for international flight operations," International Civil Aviation Organization (ICAO), accessed Dec. 15, 2023. https://www.icao.int/Newsroom/Pages/States-adopts-netzero-2050-aspirational-goal-for-international-flight-operations.aspx.

[3] Dahal, K., Brynolf, S., Xisto, C., Hansson, J., Grahn, M., Grönstedt, T., and Lehtveer, M., 2021, "Techno-economic review of alternative fuels and propulsion systems for the aviation sector," *Renewable and Sustainable Energy Reviews*, **151**, p. 111564. https://doi.org/10.1016/j.rser.2021.111564.

[4] Meher-Homji, C. B., and Prisell, E., 2000, "Pioneering Turbojet Developments of Dr. Hans Von Ohain-From the HeS 1 to the HeS 011," *J Eng Gas Turbine Power*, **122**(2), pp. 191-201. https://doi.org/10.1115/1.483194.

[5] Contreras, A., 1997, "Hydrogen as aviation fuel: A comparison with hydrocarbon fuels," *Int J Hydrogen Energy*, **22**(10-11), pp. 1053-1060. https://doi.org/10.1016/S03603199(97)00008-6.

[6] Maurice, L. Q., Lander, H., Edwards, T., and Harrison, W. E., 2001, "Advanced aviation fuels: a look ahead via a historical perspective," *Fuel*, **80**(5), pp. 747-756. https://doi.org/10.1016/S0016-2361(00)00142-3.

[7] Dukek, W., Ogston, A., and Winans, D., 1969, "Milestones in aviation fuels," *AIAA Aircraft Design and Operations Meeting*, Reston, Virginia, Jul. 1969. https://doi.org/10.2514/6.1969-779.

[8] Schmelcher, M., and Häßy, J., 2022, "Hydrogen fuel cells for aviation? A potential analysis comparing different thrust categories," *Proceedings of the ISABE*, Ottawa, Sep. 25-30, 2022, ISABE-2022-291.

[9] Baena Mejías, R., Saias, C. A., Roumeliotis, I., Pachidis, V., and Bacic, M., 2024, "Assessment of hydrogen gas turbine-fuel cell powerplant for rotorcraft," *Int J Hydrogen Energy*, **50**, pp. 772-783. https://doi.org/10.1016/j.ijhydene.2023.07.076.

[10] Lü, X., Qu, Y., Wang, Y., Qin, C., and Liu, G., 2018, "A comprehensive review on hybrid power system for PEMFC-HEV: Issues and strategies," *Energy Convers Manag*, **171**, pp. 1273-1291. https://doi.org/10.1016/j.enconman.2018.06.065.

Journal of Engineering for Gas Turbines and Power. Received July 03, 2024;
Accepted manuscript posted July 22, 2024. doi:10.1115/1.4066047

[11] Aerospace Technology Institute (ATI), 2022, "Fuel cells roadmap report," Technical Report No. FZO-PPN-COM-0033.

[12] Schmidt, T. J., and Baurmeister, J., 2008, "Properties of high-temperature PEFC Celtec®-P 1000 MEAs in start/stop operation mode," *J Power Sources*, **176**(2), pp. 428-434. https://doi.org/10.1016/J.JPOWSOUR.2007.08.055.

[13] Whatley, K. F., 1962, "American airlines experience with turbojet/turbofan engines," *Proceedings of the ASME 1962 Gas Turbine Power Conference and Exhibit*, Houston, Texas, March 4-8, 1962. https://doi.org/10.1115/62-GTP-16.

[14] Agyekum, E. B., Ampah, J. D., Wilberforce, T., Afrane, S., and Nutakor, C., 2022, "Research progress, trends, and current state of development on PEMFC-New insights from a bibliometric analysis and characteristics of two decades of research output," *Membranes*, **12**(11), p. 1103. https://doi.org/10.3390/MEMBRANES12111103.

[15] Haider, R., Wen, Y., Ma, Z., Wilkinson, D. P., Zhang, L., Yuan, X., Song, S., et al., 2021, "High temperature proton exchange membrane fuel cells: progress in advanced materials and key technologies," *Chem Soc Rev*, **50**(2), pp. 1138-1187. https://doi.org/10.1039/D0CS00296H.

[16] Branco, C. M., Sharma, S., Madalena de Camargo Forte, M., and Steinberger-Wilckens, R., 2016, "New approaches towards novel composite and multilayer membranes for intermediate temperature-polymer electrolyte fuel cells and direct methanol fuel cells," *J Power Sources*, **316**, pp. 139-159. https://doi.org/10.1016/J.JPOWSOUR.2016.03.052.

[17] Fuel Cells and Hydrogen 2 Joint Undertaking, 2020, "Hydrogen-powered aviation: a fact-based study of hydrogen technology, economics, and climate impact by 2050," EU Publications Office. https://data.europa.eu/doi/10.2843/471510.

[18] Kösters, T. L., Liu, X., Kožulović, D., Wang, S., Friedrichs, J., and Gao, X., 2022, "Comparison of phase-change-heat-pump cooling and liquid cooling for PEM fuel cells for MW-level aviation propulsion," *Int J Hydrogen Energy*, **47**(68), pp. 29399-29412. https://doi.org/10.1016/j.ijhydene.2022.06.235.

[19] Mohapatra, S. C., and Loikits, D., 2005, "Advances in liquid coolant technologies for electronics cooling," *Semiconductor Thermal Measurement and Management IEEE Twenty First Annual IEEE Symposium:* pp. 354-360, San Jose, California, 2005. https://doi.org/10.1109/STHERM.2005.1412204.

[20] Therminol, 2023, "Fluid Selection Resources," Therminol, accessed Dec. 15, 2023. https://www.therminol.com/resources/fluid-selection.

[21] Dynalene, 2023, "Heat Transfer Fluids," Dynalene, accessed Dec. 15, 2023. https://www.dynalene.com/heat-transfer-fluids/.

[22] Jadeja, K. M., Bumataria, R., and Chavda, N., 2023, "Nanofluid as a coolant in internal combustion engine - a review," *International Journal of Ambient Energy*, **44**(1), pp. 363-380. https://doi.org/10.1080/01430750.2022.2127891.

[23] Zakaria, I., Michael, Z., Mohamed, W. A. N. W., Mamat, A. M. I., Azmi, W. H., Mamat, R., and Saidur, R., 2015, "A review of nanofluid adoption in Polymer Electrolyte Membrane (PEM) fuel cells as an alternative coolant," *Journal of Mechanical Engineering and Sciences*, **8**, pp. 1351-1366. https://doi.org/10.15282/jmes.8.2015.10.0132.

[24] Yang, Y., Oztekin, A., Neti, S., and Mohapatra, S., 2012, "Particle agglomeration and properties of nanofluids," *Journal of Nanoparticle Research*, **14**(5), p. 852. https://doi.org/10.1007/s11051-012-0852-2.

[25] Shell, 2023, "Civil Jet Fuel", Shell, accessed Dec. 15, 2023. https://www.shell.com/business-customers/aviation/aviation-fuel/civil-jet-fuel-grades.html.

[26] Barron, S., 1952, "Low-Temperature Lubrication of Aircraft Engines," SAE Technical Paper 520224, https://doi.org/10.4271/520224.

[27] ESF E-33MAX Consultation, 2007, "Equivalent Safety Finding on CS 25.981: Fuel Tank Ignition Prevention – A Hot Surface Ignition Temperature," European Union Aviation Safety Agency.

[28] Federal Aviation Administration, 2018, "Fuel Tank Ignition Source Prevention Guidelines," Advisory Circular No. AC 25.981-1D.

[29] Mueller, S. A., Kim, B. R., Anderson, J. E., Kumar, M., and Huang, C., 2023, "Leaching of ions from fuel cell vehicle cooling system and their removal to maintain low conductivity," SAE Technical Paper 2003-01-0802. https://doi.org/10.4271/2003-01-0802.

[30] Mouromtseff, I. E., 1942, "Water and Forced-Air Cooling of Vacuum Tubes Nonelectronic Problems in Electronic Tubes," *Proceedings of the IRE*, **30**(4), pp. 190-205. https://doi.org/10.1109/JRPROC.1942.234654.

[31] Bonilla, C. F., 1957, "Nuclear Engineering," McGraw Hill, New York.

[32] Lenert, A., Nam Y., and Wang, E. N., 2012, "Heat Transfer fluids," *Annual Review of Heat Transfer*, **15**(15), pp. 93-129. https://doi.org/10.1615/AnnualRevHeatTransfer.2012004122.

[33] Ehrenpreis, C., El Bahi, H., Xu, H., Roux, G., Kneer, R., and Rohlfs, W., 2020, "Physically-motivated Figure of Merit (FOM) assessing the cooling performance of fluids suitable for the direct cooling of electrical components," *19th IEEE Intersociety Conference on Thermal and Thermomechanical Phenomena in Electronic Systems (ITherm):* pp. 422-429, Orlando, Florida, 2020. https://doi.org/10.1109/ITherm45881.2020.9190343.

[34] Ghajar, A., Tang, W-C., and Beam, J., 1994, "Comparison of hydraulic and thermal performance of PAO and Coolanol 25R liquid coolants," *6th Joint Thermophysics and Heat Transfer Conference*, Reston, Virginia, 1994. https://doi.org/10.2514/6.1994-1965.

[35] Green, C. E., Fedorov, A. G., and Joshi, Y. K., 2009, "Scaling analysis of performance trade-offs in electronics cooling," *Proceedings of the ASME 2009 InterPACK Conference*: pp. 1047-1056. San Francisco, California, Jul. 19-23, 2009. https://doi.org/10.1115/InterPACK2009-89389.

[36] White, F. M., 2021, "Fluid mechanics," 9th ed., McGraw Hill, New York.

[37] Baird, D. and Ferentinos, J., 1998, "Application of MIL-C-87252 in F-22 Liquid Cooling System," SAE Technical Paper 981543. https://doi.org/10.4271/981543.

[38] Dow, 2023, "Lubricants, Heat Transfer and Deicing Fluids," Dow, accessed Dec. 15, 2023. https://www.dow.com/en-us/product-technology/pt-lubricants.html.

[39] Radco, 2023, "Heat Transfer Fluids," Radco, accessed Dec. 15, 2023. https://www.radcoind.com/heat-transfer-fluids/.

[40] NIST, 2023, "NIST Chemistry WebBook," NIST Standard Reference Database Number 69, accessed Dec. 15, 2023. https://doi.org/10.18434/T4D303.

[41] Asli, M., König, P., Sharma, D., Pontika, E., Huete, J., Konda, K. R., Mathiazhagan, A., et al., 2024, "Thermal management challenges in hybrid-electric propulsion aircraft," *Progress in Aerospace Sciences*, **144**, p. 100967. https://doi.org/10.1016/j.paerosci.2023.100967.

[42] Mayhew, Y. R. and Rogers, G. F. C., 2013, "Thermodynamic and transport properties of fluids: SI units," 5th ed., Wiley Blackwell, Chichester.

[43] Kays, W. M. and London, A. L., 1984, "Compact Heat Exchangers," 3rd ed., McGraw-Hill, New York.

[44] Churchill, S. W., 1977, "Comprehensive correlating equations for heat, mass and momentum transfer in fully developed flow in smooth tubes," *Industrial & Engineering Chemistry Fundamentals*, **16**(1), pp. 109-116. https://doi.org/10.1021/i160061a021.

[45] Eaton, 2023, "Engine Fuel Pumps," Eaton, accessed Dec. 15, 2023. https://www.eaton.com/Eaton/ProductsServices/Aerospace/Fuel/index.htm.

[46] Lukaczyk, T. W., Wendroff, A. D., Colonno, M., Economon, T. D., Alonso, J. J., Orra, T. H., and Ilario, C., 2015, "SUAVE: An open-source environment for multi-fidelity conceptual vehicle design," *16th AIAA/ISSMO Multidisciplinary Analysis and Optimization Conference*, Reston, Virginia, Jun. 2015. https://doi.org/10.2514/6.2015-3087.

[47] Sinsay, J., Alonso, J., Kontinos, D., Melton, J., and Grabbe, S., 2012, "Air vehicle design and technology considerations for an electric VTOL metro-regional public transportation system," *12th AIAA Aviation Technology, Integration, and Operations (ATIO) Conference and 14th AIAA/ISSMO Multidisciplinary Analysis and Optimization Conference*, Reston, Virginia, Sep. 2012. https://doi.org/10.2514/6.2012-5404.

[48] Meredith, F. W., 1935, "Cooling of aircraft engines with special reference to ethylene glycol radiators enclosed ducts," Technical Report No. 1683.

[49] Drela, M., 1995, "Aerodynamics of heat exchangers for high-altitude aircraft," *13th Applied Aerodynamics Conference*, Reston, Virginia, Jun. 1995. https://doi.org/10.2514/6.1995-1866.

[50] Steinke, M. E. and Kandlikar, S. G., 2006, "Single-phase liquid friction factors in microchannels," *International Journal of Thermal Sciences*, **45**(11), pp. 1073-1083. https://doi.org/1016/j.ijthermalsci.2006.01.016.

[51] Yunus, C. and Ghajar, A., 2020, "Heat and mass: fundamentals and applications," 6th ed., McGraw-Hill Education, New York.

[52] PowerCell Group, 2023, "Enabling hydrogen electric airplanes," PowerCell Group, accessed Dec. 15, 2023. https://powercellgroup.com/segments/aviation/.

[53] Barbir, F., 2005, "Proton Exchanger Membrane Fuel Cells: Theory and Practice," Academic Press. https://doi.org/10.1016/B978-0-12-078142-3.X5000-9.

[54] Bargal, M. H. S., Abdelkareem, M. A. A., Tao, Q., Li, J., Shi, J., and Wang, Y., 2020, "Liquid cooling techniques in proton exchange membrane fuel cell stacks: A detailed survey," *Alexandria Engineering Journal*, **59**(2), pp. 635-655. https://doi.org/10.1016/j.aej.2020.02.005.

[55] Yoshida, T. and Kojima, K., 2015, "Toyota MIRAI fuel cell vehicle and progress toward a future hydrogen society," *The Electrochemical Society Interface*, **24**(2), pp. 45-49. https://doi.org/10.1149/2.F03152if.

[56] Hashmi, S. M. H., "Cooling strategies for proton exchange membrane fuel cell stacks," PhD Thesis, Helmut-Schmidt-Universität, Hamburg, Germany, 2010. https://doi.org/10.24405/396.

[57] Ugbeh-Johnson, J. and Carpenter, M., 2023, "The impact of sustainable aviation fuels on aircraft fuel line ice formation and pump performance," *The Aeronautical Journal*, **127**(1314), pp. 1287-1307. https://doi.org/10.1017/aer.2023.6.

[58] Ugbeh-Johnson J., Carpenter, M., Williams, C., Pons, J-F. and McLaren, D., 2022, "Complexities associated with nucleation of water and ice from jet fuel in aircraft fuel systems: A critical review," *Fuel*, **310**, p. 122329. https://doi.org/10.1016/j.fuel.2021.122329.

[59] Fly, A. and Thring, R. H., 2016, "A comparison of evaporative and liquid cooling methods for fuel cell vehicles," *Int J Hydrogen Energy*, **41**(32), pp. 14217-14229. https://doi.org/10.1016/j.ijhydene.2016.06.089.

[60] Fronk, M. H., Wetter, D. L., Masten, D. A., and Bosco, A., 2000, "Proton exchange membrane fuel cell system solutions for transportation," *SAE Transactions*, **109**, pp. 212-219. https://www.jstor.org/stable/44745837.

[61] Kellermann, H., Habermann, A. L. and Hornung, M., 2019, "Assessment of aircraft surface heat exchanger potential," *Aerospace*, **7**(1), p. 1. https://doi.org/10.3390/aerospace7010001.

[62] Greatrix, D. R., 2012, "Powered Flight," 1st ed, Springer, London. https://doi.org/10.1007/978-1-4471-2485-6.

[63] Liu, Q., Xu, H., Lin, Z., Zhu, Z., Wang, H. and Yuan, Y., 2023, "Experimental study of the thermal and power performances of a proton exchange membrane fuel cell stack affected by the coolant temperature," *Appl Therm Eng*, **225**, p. 120211. https://doi.org/10.1016/j.applthermaleng.2023.120211.

[64] Topuz, A., Engin, T., Erdoğan, B., Mert, S., and Yeter, A., 2020, "Experimental investigation of pressure drop and cooling performance of an automobile radiator using Al2O3-water+ethylene glycol nanofluid," *Heat and Mass Transfer*, **56**(10), pp. 2923-2937. https://doi.org/10.1007/s00231-020-02916-8.

[65] Montgomery, D. C., 2013, "Design and analysis of experiments," 8th ed., John Wiley & Sons Inc.

[66] Antony, J., 2003, "Design of experiments for engineers and scientists," Butterworth-Heinemann, Oxford.

[67] Schröder, M., Becker, F. and Gentner, C., 2024, "Optimal design of proton exchange membrane fuel cell systems for regional aircraft," *Energy Convers Manag*, **308**, p. 118338. https://doi.org/10.1016/j.enconman.2024.118338.

[68] Chang, Y-J., Chang, W-J., Li, M-C. and Wang, C-C., 2006, "An amendment of the generalized friction correlation for louver fin geometry," *Int J Heat Mass Transf*, **49**(21-22, pp. 4250-4253. https://doi.org/10.1016/j.ijheatmasstransfer.2006.05.011.

[69] Chang, Y-J. and Wang, C-C., 1997, "A generalized heat transfer correlation for louver fin geometry," *Int J Heat Mass Transf*, **40**(3), pp. 533-544. https://doi.org/10.1016/0017-9310(96)00116-0.

[70] Baehr, H. D. and Stephan, K., 2013, "Heat and Mass Transfer," 1st ed., Springer, Heidelberg. https://doi.org/10.1007/978-3-662-03659-4.

Journal of Engineering for Gas Turbines and Power. Received July 03, 2024;
Accepted manuscript posted July 22, 2024. doi:10.1115/1.4066047

Table Caption List

Table 1 Critical system level requirements for liquid coolants inside a fuel cell powered aircraft.

Table 2 Comparison of proposed figure of merits.

Table 3 System model boundary conditions for coolant selection.

Table 4 Full factorial Design of Experiments with two levels to determine the sensitivity of total mass and total power to uncertain boundary conditions.

Table 5 Liquid coolant use cases.

Table 6 Boundary conditions used for both the radiator sizing models.

Figure Captions List

Fig. 1 Schematic of a Proton Exchange Membrane Fuel Cell (PEMFC) and the electrochemical reaction.

Fig. 2 Notional liquid cooled proton exchange membrane fuel cell propulsion system with a ducted radiator installed under the wing.

Fig. 3 Coolant ontology. Note – Aliphatic and Aromatic Hydrocarbons may comprise blends, and ‘Other HC’ categorizes Hydrocarbons of unknown composition.

Fig. 4 (a) Figure of Merit for coolant categories spanning their operating temperature at atmospheric pressure. The dashed line encompasses all of

Journal of Engineering for Gas Turbines and Power. Received July 03, 2024;
Accepted manuscript posted July 22, 2024. doi:10.1115/1.4066047

the Hydrocarbons. (b) Magnification of the Hydrocarbons which identifies Aliphatics, Aromatics, and Other HCs. *Refer to Table 1.

Fig. 5 (a) Integrated average Figure of Merit for coolant categories and (b) their operating temperature range. *Refer to Table 1.

Fig. 6 (a) A schematic of the system model including the radiator, stack, piping, coolant and pump. (b) A flowchart of the system model which includes the iterative radiator sizing algorithm.

Fig. 7 A schematic of radiator geometry (11.32-0.737-SR) with the respective correlations. *[43], **[36], and †[44].

Fig. 8 Percent contribution of the model terms on (a) total mass and (b) total power. derived from a full factorial Design of Experiment for an Aliphatic coolant. Up to 95% of the percent contribution is included.

Fig. 9 Pareto fronts at 80°C for (a) and (b), and 200°C for (c) and (d). Total power versus total mass: (a) and (c). Pumping power versus total mass: (b) and (d). Normalized by deionized water at 80°C. Excludes low temperature threshold.

Fig. 10 Pareto efficient coolants for 80–200°C. (a) Normalized total power versus Normalized total mass. (b) Magnification of (a). (c) Normalized pumping power versus Normalized total mass. The number labels correspond to the operating temperature.

Journal of Engineering for Gas Turbines and Power. Received July 03, 2024;
Accepted manuscript posted July 22, 2024. doi:10.1115/1.4066047

Fig. 11 Pareto efficient coolants for 80–200°C. (a) Normalized total power versus Normalized total mass. (b) Magnification of (a). The number labels correspond to the operating temperature.

Fig. 12 Cases for selecting suitable coolants. The requirements from Table 1 are applied.

Fig. 13 Comparison of the radiator sizing model with 50-50% EG-W to [67]. Dry radiator core mass versus coolant inlet temperature.